

Room-temperature ferroelectric, piezoelectric and resistive switching behaviors of single-element Te nanowires

Received: 23 April 2024

Accepted: 26 August 2024

Published online: 02 September 2024

 Check for updates

Jinlei Zhang ^{1,2,3,17}, Jiayong Zhang^{1,17}, Yaping Qi ^{4,5,17}, Shuainan Gong^{1,17}, Hang Xu¹, Zhenqi Liu¹, Ran Zhang¹, Mohammad A. Sadi⁶, Demid Sychev⁶, Run Zhao¹, Hongbin Yang⁷, Zhenping Wu⁸, Dapeng Cui⁹, Lin Wang¹⁰, Chunlan Ma¹, Xiaoshan Wu ², Ju Gao^{1,11}, Yong P. Chen^{5,6,12} , Xinran Wang ^{13,14,15,16}  & Yucheng Jiang^{1,2} 

Ferroelectrics are essential in memory devices for multi-bit storage and high-density integration. Ferroelectricity mainly exists in compounds but rare in single-element materials due to their lack of spontaneous polarization in the latter. However, we report a room-temperature ferroelectricity in quasi-one-dimensional Te nanowires. Piezoelectric characteristics, ferroelectric loops and domain reversals are clearly observed. We attribute the ferroelectricity to the ion displacement created by the interlayer interaction between lone-pair electrons. Ferroelectric polarization can induce a strong field effect on the transport along the Te chain, giving rise to a self-gated ferroelectric field-effect transistor. By utilizing ferroelectric Te nanowire as channel, the device exhibits high mobility ($\sim 220 \text{ cm}^2 \cdot \text{V}^{-1} \cdot \text{s}^{-1}$), continuous-variable resistive states can be observed with long-term retention ($>10^5 \text{ s}$), fast speed ($<20 \text{ ns}$) and high-density storage ($>1.92 \text{ TB/cm}^2$). Our work provides opportunities for single-element ferroelectrics and advances practical applications such as ultrahigh-density data storage and computing-in-memory devices.

Low-dimensional ferroelectrics, with spontaneous charge polarizations tunable by external electric fields, have drawn extensive interest in nanoelectronics, for applications such as transistors, memories, and sensors^{1–3}. The direction of the spontaneous polarization is important to determine possible applications. The out-of-plane ferroelectricity is preferred to realize memory miniaturization with high integration density and low power consumption^{4–6}, compared with the in-plane one. Usually, ferroelectrics are insulators with low carrier mobility and large band gaps^{1,5–9}. For functional nanodevices, an effective strategy is to construct heterostructures by combining ferroelectric gate insulators and channel semiconductors^{10–16} to make ferroelectric field-effect transistors (Fe-FETs). However, leakage current and charge trapping usually exist at the interface, limiting application prospects. A material that is both a high-mobility semiconductor and out-of-plane ferroelectric could make an ideal transistor/memory nanodevice and

overcome the above disadvantages^{17–20}. Such a material requires a highly anisotropic lattice structure with different properties. Recently, a two-dimensional (2D) ferroelectric semiconductor $\alpha\text{-In}_2\text{Se}_3$ has been used as the channel material to compose a Fe-FET¹⁷. The spontaneous out-of-plane polarization can tune the in-plane electronic transport via a gate voltage to give rise to a nonvolatile resistive switching, achieving a self-gated Fe-FET (SF-FET). Until now, many efforts have been made to explore ferroelectric semiconductors using compound 2D materials (such as $\alpha\text{-In}_2\text{Se}_3$)^{17,18,21} and emerging moiré superlattices (such as twisted MoS_2 bilayers)^{19,22,23}.

Ferroelectricity is mainly found in compounds with non-centrosymmetric structures^{18,22–28}, which are unexpected in elemental crystals. Generally, elemental materials possess centrosymmetric structures without local electronegativity differences, thereby lacking spontaneous electric polarizations^{7,28,29}. To date, it has been a challenge

A full list of affiliations appears at the end of the paper.  e-mail: yongchen@purdue.edu; xrwang@nju.edu.cn; jyc@usts.edu.cn

to realize single-element ferroelectrics. Recently, tellurium (Te) has drawn significant interest as a 2D single-element semiconductor^{30,31}, due to its outstanding electrical conductivity^{32–34}, one-dimensional chain structure^{35–37}, and strong spin–orbit coupling (SOC)^{38,39}. Theories have predicted that layered Te possesses a broken symmetry and can be a ferroelectric semiconductor⁷. The interlayer interaction between adjacent Te chains drives the atomic displacement accompanied by charge transfer, separating the charge centers and leading to spontaneous electric polarization. However, until now, there has been no experimental evidence to support such a prediction. Most recent studies have focused on the Te nanosheets⁴⁰, whose highly stable structure and strong electrostatic screening may limit the reversal of dipoles. Another form of Te is the nanowire with a relatively low barrier height of atomic displacement^{41,42}, providing a possible route to achieve ferroelectricity.

In this work, we report room-temperature vertical ferroelectricity in quasi-one-dimensional Te nanowires and at the edges of Te nanosheets. The ferroelectric hysteresis and domain switching are observed by piezoresponse force microscopy (PFM). Using spherical aberration corrected scanning transmission electron microscopy (Cs-corrected STEM), we attribute the vertical ferroelectricity to the atomic displacement perpendicular to the atomic chains within Te nanowires, verified by density functional theory (DFT) calculations. Furthermore, the Te nanowire can be used as a ferroelectric semiconductor channel to construct a SF-FET with a *h*-BN gate dielectric. By adjusting the remnant polarization (P_r) of Te nanowires to regulate their vertical depolarization field, SF-FETs exhibit continuous-variable resistive states with fast speed and high-density storage. These capabilities offer a solution for in-memory computing, particularly in artificial intelligence applications that leverage ferroelectric properties.

Results

Quasi-one-dimensional Te nanowires were synthesized with a width of 30–300 nm and a height of 5–30 nm using a substrate-free solution method (section “Methods” and Supplementary Fig. 1), and were identified by Raman spectra (Supplementary Fig. 2a). The surface

morphology and cross section of a representative Te nanowire probed through atomic force microscopy (AFM) and scanning electron microscopy (SEM) are shown in Fig. 1a. It shows a triangle-like cross section with clean surfaces and neat edges, indicating the high crystal quality. The STEM image shows a unique chiral chain lattice in Fig. 1b. Each Te atom is bonded to two nearest neighbors, forming helical chains along the *c*-axis direction (which is the long axis of the nanowire). Those chains are stacked in a hexagonal array through van der Waals bonds between adjacent atomic chains. Note that the Te nanowire shows an inclined plane along the *b*-axis at the edge. It can be thought to be formed by multiple Te atomic layers stacked along the \bar{e} direction (perpendicular to *b*-*c* plane). Layer-center atoms (LCAs) in each single Te chain show relative off-center displacements, thereby giving rise to a non-centrosymmetric lattice structure of the inclined plane at the edge (the right in Fig. 1b and Supplementary Notes 1, 2). As is well known, the breaking of symmetry is an important premise of ferroelectricity.

Considering the experimental case, we used DFT to simulate the ferroelectric characteristics of few-layer Te (Supplementary Table S1 and Note 3), focusing on modeling the off-center displacement of LCAs at the inclined edge (which as discussed below would give a vertical polarization component measured in our experiment). To model the layers near and parallel to the inclined edge and stacked along the \bar{e} direction of the Te nanowire, we performed detailed calculations for a 4-layer (4L) Te sheet in three different states. The atomic structures of the α -, β -, and α' -state in a 4L Te are plotted in the left, middle, and right insets in Fig. 1c, respectively. The β -state Te has the space group $P2_1/m$ and is centrosymmetric, while the space group of the α (α')-state Te is reduced to $P2_1$. The α - and α' -states Te are energetically degenerate with the opposite displacement (about ± 0.41 Å) of their LCAs. The climbing nudged elastic band (NEB) calculations show that the two stable structures of non-centrosymmetric α - and α' -state are connected through an extremum energy point with the centrosymmetric β -state, implying the possible existence of ferroelectricity. The calculated ferroelectric switching pathway of 4L Te from α - to α' -state in Fig. 1c shows that the energy barrier between the non-

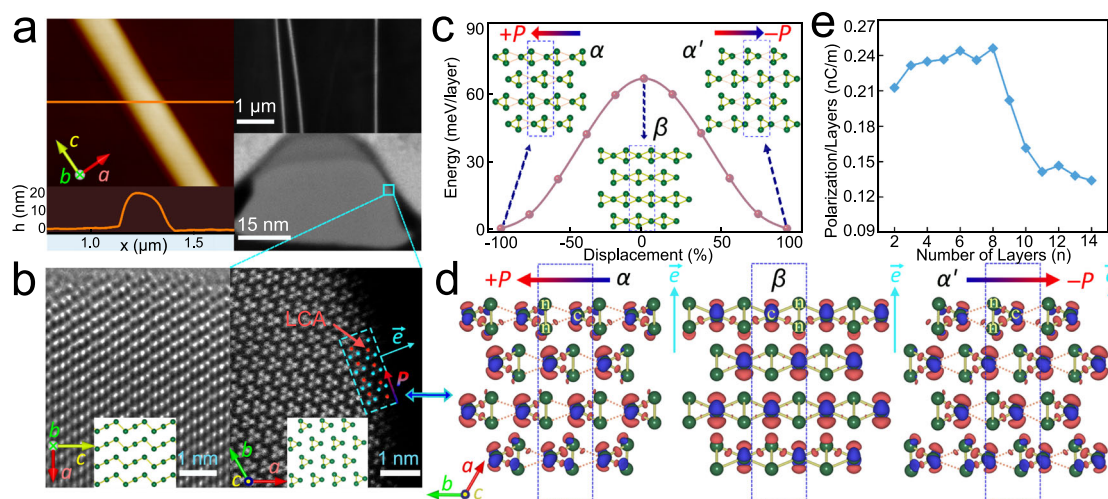


Fig. 1 | Polar structure and ferroelectric polarization. **a** AFM, SEM, TEM topographical images and the AFM height profile of a Te nanowire on a SiO_2/Si wafer. **b** STEM images of the Te nanowire viewed along *b*- and *c*-axes (lower left insets here as well as in (a) show axes projected into the image planes; left and right insets show atomic lattice models). *e* is the epitaxial direction of inclined stepwise planes. **c** Ferroelectric switching pathway of 4L Te from α - to α' -state calculated using the NEB method. Insets display the atomic structures of α and α' , representing two opposite polarization states, as well as the paraelectric nonpolar β -state. **d** Differential charge density ($\Delta\rho$) of 4L Te for α -, β - and α' -states. Here

$\Delta\rho = \rho(\text{tot}) - \rho(c\text{-Te}) - \rho(n\text{-Te})$, where $\rho(\text{tot})$ is the total charge density, $\rho(c\text{-Te})$ is the charge density of the LCAs (c) and $\rho(n\text{-Te})$ is the charge density of the neighboring (n) Te atoms. Red and blue colors represent the charge accumulation and depletion, respectively. The isosurface values in α - (α' -) and β -states are set to 0.007 and 0.006 e/bohr^3 , respectively. The arrows denote the polarization direction. Dotted rectangular boxes in (c) and (d) indicate the smallest repeatable unit in the periodic lattice. **e** Calculated polarization per layer for the α -state Te with different number of layers.

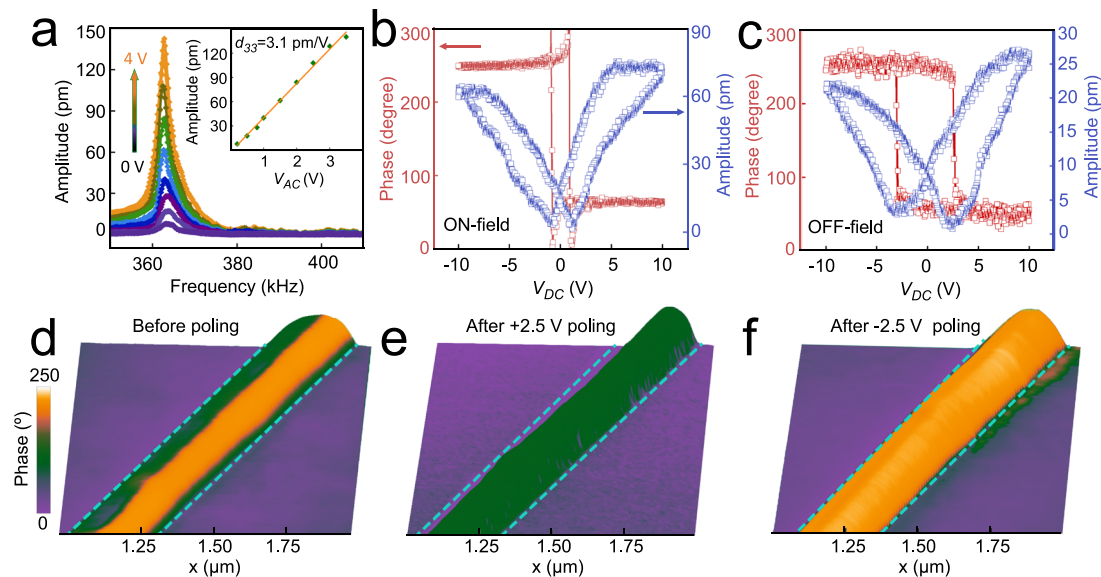


Fig. 2 | Ferroelectric hysteresis and domain switching. **a** Piezoresponse vs frequency under different V_{AC} for the Te nanowire on an Au-coated silicon substrate, measured at a representative location on the inclination edge, showing a resonance peak around 365 kHz. Inset shows the linear dependence of piezoresponse amplitude on V_{AC} with an effective piezoelectric coefficient d_{33} of -3.1 pm/V. Phase-voltage hysteresis loops and amplitude-voltage butterfly loops measured by vertical ON-field (**b**) and OFF-field (**c**) PFM, where DC bias voltage (V_{DC}) is applied

to the tip before (“OFF-field”) or during (“ON-field”) the AC drive. Phase mapping (OFF-field) measured by vertical PFM before electric poling (**d**), after poling at $+2.5$ V (**e**), and after poling at -2.5 V (**f**), overlaid on the 3D topography image of the nanowire (width ~ 300 nm, thickness ~ 18.9 nm). The area of Te nanowire is marked by the cyan dashed line. $V_{DC} = 0$ V for (**a**) and (**b–f**) were measured with $V_{AC} = 1.5$ V driving on the resonance frequency.

centrosymmetric and centrosymmetric states is about 67 meV/layer. We also calculated energy barriers for different numbers of Te layers (Supplementary Fig. 3). The differential charge densities are calculated to investigate the physical mechanism of the existence of polarization in the α - and α' -states Te (Fig. 1d), with the red and blue colors denoting the electron density charge accumulation and depletion regions, respectively. For the β -state 4L Te, the charge distribution is centrosymmetric around the LCAs, resulting in the positive and negative charge centers canceling each other to give a zero net polarization. In contrast, the differential charge densities of the α - and α' -states show charge redistributions between the LCAs and their neighboring atoms. For the α - (or α' -) state layered Te, the negative charge center moves to the right (or left) side of the positive charge center due to more charge accumulating at the right (or left), resulting in the emergence of nonzero polarization pointing from right (or left) to left (or right). Figure 1e shows the calculated spontaneous polarization per layer as a function of the number of layers for α -state Te. We do not calculate a monolayer as it has only the β -state as the stable state and it alone cannot make a meaningful nanowire with inclined edges⁷. The 2D polarization density is about $(2.1\text{--}2.4) \times 10^{-10}$ C/m per layer and slightly increases with increasing number of layers below 8 layers. Apparently, the polarization starts to decrease with further increasing number of layers beyond 8 layers. Our calculations strongly support the existence of ferroelectricity within the layer (perpendicular to the Te chains), thus along the b -axis of the single-element Te nanowire giving rise to a vertical (perpendicular to the a - c plane and substrate) polarization component. Given that Te nanowires are van der Waals materials with one-dimensional chain structures, their crystal structures along both the a -axis and b -axis can be likened to stacked layers of Te atoms, exhibiting the similar atomic arrangements. Our few-layer model can apply to the Te layers parallel to the a direction (e.g., near the bottom surface of the Te nanowire), implying a polarization along the a -axis can also exist. However, as the number of Te atomic layers increases along either the a -axis or b -axis, the bandgap of Te decreases, posing challenges to sustaining spontaneous polarization. A narrow bandgap can induce electrostatic screening due to high carrier density, leading

to the disappearance of the depolarization field and hindering the maintenance of ferroelectric polarization.

Vertical PFM was performed to investigate the spontaneous electric polarization of the Te nanowire. Te nanowires were transferred onto an Au-coated silicon substrate for the contact-mode PFM measurement. Figure 2a obtained on a representative Te nanowire, shows that the piezoresponse peaks at a resonance frequency of ~ 365 kHz, and the intensity is linear with the amplitude of the AC drive voltage (V_{AC}) as shown in the inset in Fig. 2a. It verifies the existence of electric dipole moment and piezoelectricity with an effective piezoelectric coefficient d_{33} of ~ 3.1 pm/V in the Te nanowire. Both phase hysteresis and butterfly amplitude loops are observed in Fig. 2b, c, respectively. ON- and OFF-field PFM method is used to identify the ferroelectricity (Supplementary Fig. 2b and Note 4), which shows the typical hysteresis shapes caused by the switching of ferroelectric domains²⁰. In addition, various driving voltage (V_{AC}) (Supplementary Fig. 4 and Note 5) and opposite poling voltages (Supplementary Fig. 5 and Note 6) are employed to entirely preclude the interference of the charge adsorption/desorption process in PFM measurements. The thickness dependence of ferroelectricity is studied (Supplementary Fig. 6 and Note 7). It is important to clarify that the thickness refers to the height of Te nanowires, which directly corresponds to the vertical measurement scale at the boundary of the Te nanowire/nanosheet. Considering the layered structure of Te nanowires along the a - c plane, this height to some extent corresponds to the number of layers. It is found that the ferroelectricity of Te nanowire decreases with increasing thickness and vanishes at thickness over 49 nm. This is due to the narrowing of its bandgap, which leads to higher carrier density and induces electrostatic screening, preventing the observance of ferroelectric polarization. For comparison, Te nanowires were also transferred to an N -doped conductive silicon substrate to exclude the possible effect of substrates, showing a similar ferroelectric hysteresis (Supplementary Fig. 7). PFM is used to identify the distribution of polarization within the Te nanowire, reflecting its local ferroelectric domain structure (Fig. 2d). The phase and amplitude mappings correspond well to each other, overlaid on the three-dimensional (3D) topography (Fig. 2d and

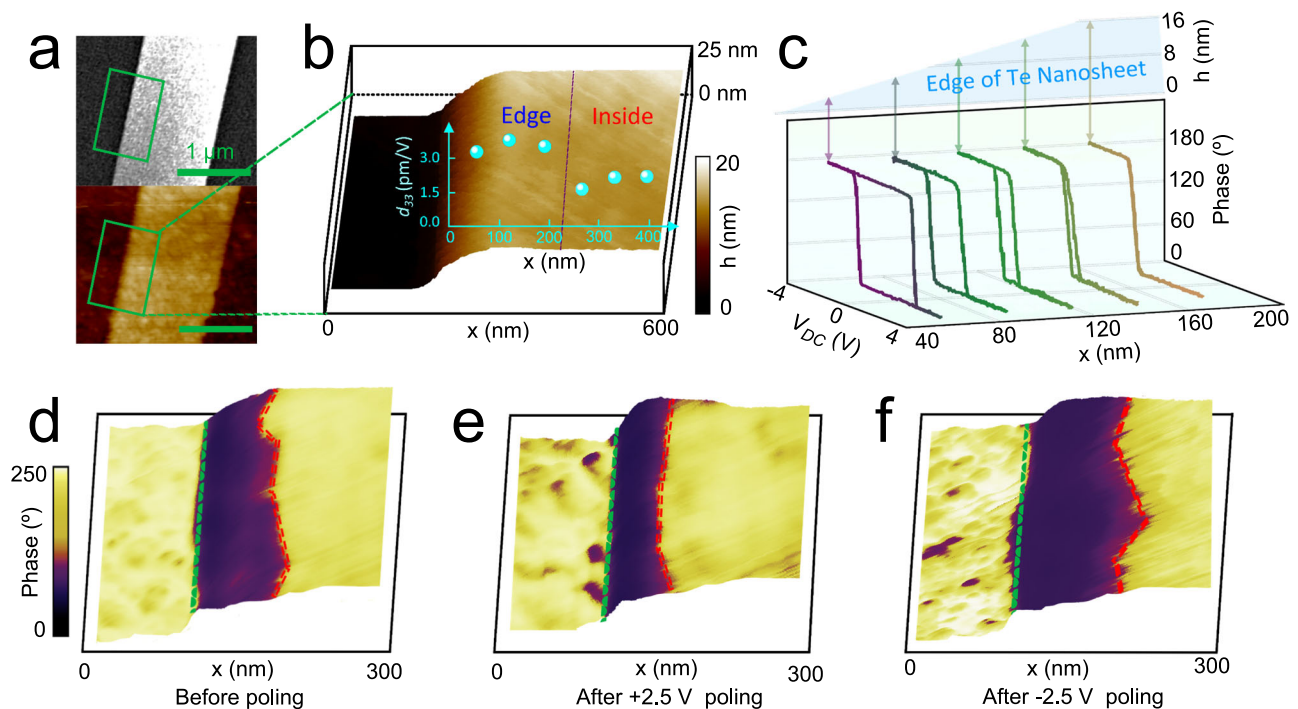


Fig. 3 | Edge ferroelectricity in a Te nanosheet. **a** Upper and lower: SEM and AFM topographical images of a Te nanosheet (height of -15 nm) on an Au-coated silicon wafer. **b** Values of d_{33} at the different marked positions (overlaid on an AFM topograph) of the Te nanosheet, showing that d_{33} at the edge is about 80% higher than that inside of the nanosheet. **c** OFF-field PFM phase hysteresis loops from the edge to the inside of 2D Te nanosheet, showing ferroelectric domain with edge

width <200 nm. Upper part is a schematic height profile of the edge and vertical arrows mark locations where individual PFM traces were measured. Vertical PFM phase mapping before electric poling (**d**), after poling at +2.5 V (**e**), after poling at -2.5 V (**f**), overlaid on 3D topography image of the Te nanosheet. **c-f** were measured with $V_{AC} = 1.5$ V driving on the corresponding local resonance frequency.

Supplementary Fig. 8). The ferroelectric domain pattern shows a strong contrast between upward (orange) and downward (olive) polarizations with domain walls along the chain direction in the Te nanowire. Such a domain structure can be attributed to the opposite off-center ion displacements between the two inclined edges (Supplementary Fig. 9). The narrow olive belt at the right edge may result from a slight bend at the end of the edge (Fig. 1a, lower right). For a ferroelectric, off-center ion displacements are tunable by mechanical or electric driving, thereby reversing the ferroelectric domains. Here, the reversal of domains is evaluated after electrical poling using a DC bias applied to the proximal tip. We investigate the reversal of the ferroelectric domain in the Te nanowire by “poling” with opposite DC bias (± 2.5 V) applied in Fig. 2e, f. It is worth noting that ferroelectricity can still be observed in Te nanowires with even narrower diameters, down to 44.9 nm (Supplementary Fig. 10). This significant reduction in scale limit for maintaining ferroelectricity can enable the achievement of ultrahigh data storage density in ferroelectric storage systems, successfully overcoming the major challenge of poor storage density. Additionally, to verify the intrinsic ferroelectricity, the broken inversion symmetry of Te nanowires/nanosheets was confirmed by SHG measurements (Supplementary Figs. 11, 12 and Note 8). It is noteworthy that the height of Te nanowire increases significantly and its shape changes after poling, which may be attributed to the nonvolatile electrostriction (Supplementary Fig. 13 and Note 9). The orientation of ferroelectric polarization is switchable with the external electric field. Our results demonstrate that the ion displacements at the inclined edge give rise to a vertical component of electric polarization that can be locally detected and controlled by an external field. The ferroelectric polarization reversal with a saturation polarization (Ps) of $-0.02 \mu\text{C}/\text{cm}^2$ was directly confirmed by measuring the typical polarization-electric field (P - E) hysteresis loop in a compressed tablet made from Te nanowires (Supplementary Fig. 14).

The origin of the ferroelectricity in Te nanowires implies the importance of the inclined edge. Besides the Te nanowire, one can synthesize Te nanosheet by a similar substrate-free solution process. Therefore, it is intriguing to investigate the usually neglected edge ferroelectric responses of Te nanosheets. Figure 3a shows the SEM and AFM images of a Te nanosheet with a width of $\sim 1.2 \mu\text{m}$ and a thickness of ~ 15 nm. An inclined edge of the Te nanosheet is shown in Fig. 3b, providing a possible platform to investigate edge ferroelectricity. It is intriguing that the effective piezoelectric coefficient (d_{33}) at the edge was found to be $\sim 80\%$ higher than that inside (Fig. 3b and Supplementary Fig. 15a). The difference in piezoelectric responses between the edge and inside is also reflected by the resonance frequencies, which are about 371 kHz (edge) and 391 kHz (inside), respectively. We note that the existence of piezoelectric resonance itself does not necessarily imply ferroelectricity. The edge electric polarization of the Te nanosheet is also investigated using the vertical PFM in Fig. 3c. The phase hysteresis loops were measured at different locations along the edge indicated by double arrows in Fig. 3c. It is observed that vertical ferroelectricity has been identified in the whole edge region. The coercive field decreases gradually as the tip climbs up the edge. The PFM phase hysteresis cannot be observed with the tip approaching the highest position, for the tip has already been placed in the inner region. Our results show that the ferroelectricity emerges only at the edge of the Te nanosheet. In comparison, for Te nanowires with a width of 20–300 nm, the top surface is full of inclined steps, causing ferroelectricity in all regions. To control the ferroelectric domain near the edge of the Te nanosheet, we used a biased tip above the local domain to apply an electric field while scanning the Te nanosheet. The PFM phase images are overlaid on 3D topography of the nanosheet after DC bias poling in Fig. 3d–f. We observe the post-poling shift of the domain wall, demonstrating the switching of ferroelectric polarization induced by

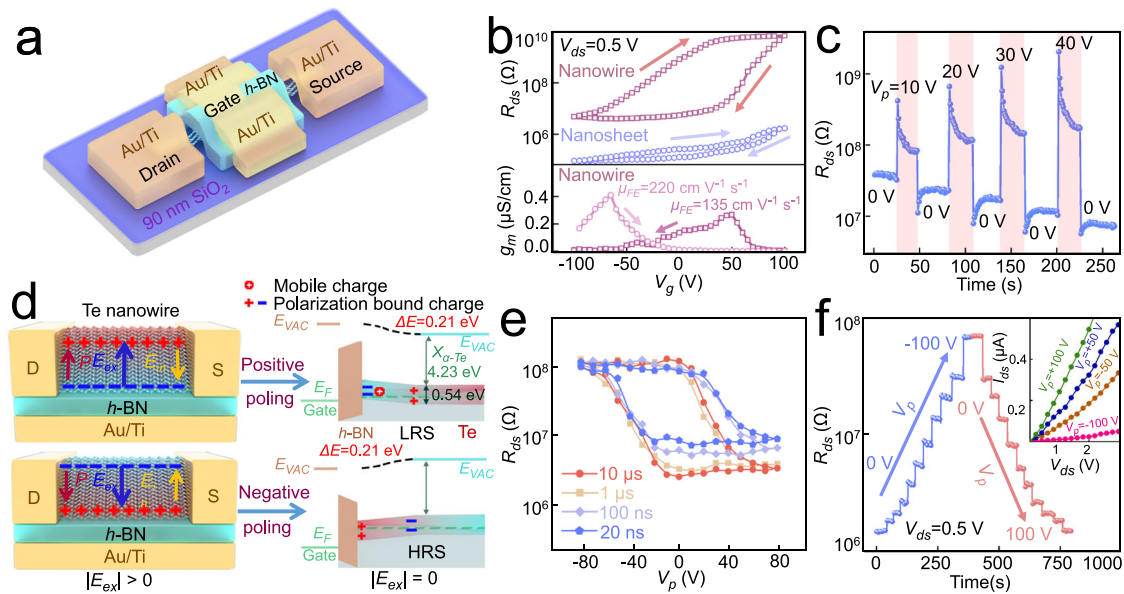


Fig. 4 | Switching characteristics exhibiting nonvolatile memory of a Te nanowire self-gated ferroelectric field-effect transistor (SF-FET). **a** Schematic showing the device structure. **b** R_{ds} - V_g characteristics for the Te nanowire and nanosheet SF-FETs (upper) and g_m - V_g hysteresis loop of Te nanowire SF-FET (lower). **c** Nonvolatile switching of R_{ds} measured after applying multiple V_p square pulses with the pulse width of 25 s, exhibiting multilevel resistive states. **d** Schematic showing polarization bound charge distribution with an external

electric field applied and band structures for LRS and HRS at zero field. **e** R_{ds} - V_p hysteresis loops at $V_{ds} = 0.5$ V. Measurement of each data point is performed at $V_g = 0$ V after waiting for 1 min following applying each V_p pulse width of 20 ns, 100 ns, 1 μ s, and 10 μ s. **f** Nonvolatile resistive states switched by different V_p . Resistive states are measured after applying V_p pulses (from -100 V to 100 V then back to -100 V in steps of 10 V) of 100 -ms width. The inset is the linear I_{ds} - V_{ds} characteristics after applying different V_p pulses labeled.

the external electric field. The dark region, corresponding to the ferroelectric domain, tends to shrink after a positive poling of $+2.5$ V (Fig. 3e), but expands after a negative poling (Fig. 3f). Due to symmetry breaking in Te nanosheets/nanowires, ferroelectric polarization primarily occurs at the boundaries, aligned along the atomic plane of surface at these boundaries. Therefore, at the edges of Te nanosheets, the ferroelectric polarization tends to align parallel to the inclined Te layer along the b -axis, forming the domains.

Given that Te is a p -type semiconductor (Supplementary Fig. 16)^{33–35,39,41,42}, a ferroelectric Te nanowire can be used as the channel material of a SF-FET via its vertical spontaneous electric polarization. Figure 4a shows a SF-FET device composed of a Te nanowire as the channel material and a h -BN layer as the top gate dielectric. The optical and STEM images of Te-nanowire and Te-nanosheet SF-FET devices are exhibited in Supplementary Figs. 17 and 18, respectively. The Te-nanowire SF-FET possesses a typical (p -type) field-effect behavior, as shown by the transfer curves in Fig. 4b and Supplementary Fig. 19, where a gate voltage (V_g) sweeps to vary the carrier density. As a reference for the transport characteristic of a transistor, effective extrinsic field-effect mobility (μ_{FE}) values of -135 and -220 $\text{cm}^2 \text{V}^{-1} \text{s}^{-1}$ for the backward and forward gate voltage sweeps, respectively, can be extracted from the maximum transconductance (g_m) (Fig. 4b, lower). These values are comparable to the high-mobility FETs based on few-layer black phosphorene⁴³ and few-layer MoS_2 ⁴⁴. It is most intriguing to observe the resistance- V_g (R_{ds} - V_g) hysteresis (Fig. 4b, upper) originating from the switching of vertical electric polarization. This provides strong evidence supporting the ferroelectricity of the Te nanowire, and suggests a potential application for resistive memories. For comparison, we have also investigated the field effect of Te nanosheet that shows a much smaller hysteresis behavior. The vertical ferroelectricity exists only at the edge, so the spontaneous polarization is not large enough to gate the entire Te nanosheet. In addition, we note that both Te nanowire and nanosheet exhibit clockwise loops in R_{ds} - V_g , different from a regular Fe-FET^{13,17}. For the self-gated device, the external electric field (E_{ex}) opposed the internal remnant electric

field (E_{in}) induced by the spontaneous polarization, thereby causing competition and balance between them. To clarify this hysteresis behavior, we studied the resistive response to multiple on/off operations of a pulsed gate voltage (V_p) as shown in Fig. 4c. It is observed that R_{ds} increases sharply when V_p is applied, but decreases to a level even lower than the initial resistance once V_p is removed (so supply voltage $V_g = 0$ V again). Additional and even lower resistive states can be obtained at zero V_g after more V_p pulses with increasing amplitudes. Further details on the resistive switching performance of SF-FET after various continuous voltage or pulsed voltage (V_p) can be found in Supplementary Figs. 20–22 and Note 11. SF-FET demonstrates excellent nonvolatile resistive switching performance, showcasing continuous-variable resistive states (>16) with good stability, long-term retention ($>10^5$ s), and fast speed (<20 ns). To interpret this effect, a schematic diagram is provided to describe the gating process and the band structures for high resistive state (HRS) and low resistive state (LRS) in Fig. 4d, where the band energy is obtained from the DFT calculations (Supplementary Figs. 23 and 24). In the case of continuous application of positive V_g or E_{ex} , the R_{ds} increase is mainly determined by E_{ex} because of $E_{ex} \gg E_{in}$. In the absence of E_{ex} , E_{in} has an opposite direction to E_{ex} , thus has a similar effect to a negative V_g or E_{ex} that attracts more mobile holes to the (p -type) channel and gives rise to R_{ds} lowering (LRS, Fig. 4d, right upper), explaining the lower R_{ds} reached after positive V_p observed in Fig. 4c. The Te SF-FET device enables a nonvolatile resistive memory with multilevel high and low resistance states. Figure 4e shows R_{ds} - V_p hysteresis loops at different pulse durations. Despite the pulse duration range of 20 ns–10 μ s, the device shows almost the same nonvolatile resistive states. It is intriguing that the fast switching was even obtained within 20 ns. Such a fast resistive switching is consistent with the speed of ferroelectric polarization reversal (≤ 20 ns), giving the strong evidence to support the vertical ferroelectricity in the whole Te nanowire⁴⁵. We have simulated the R_{ds} - V_g and R_{ds} - V_p hysteresis loops (Supplementary Fig. 25 and Note 11), which align with our experimental results. Additionally, the measurement of the depolarization field (Supplementary Fig. 26 and

Note 12), the P_r in Te nanowires (with a thickness of ~24 nm) is $-0.026 \mu\text{C}/\text{cm}^2$. P_r - V_p hysteresis loops were also measured by varying the temperature and pulse amplitudes (Supplementary Fig. 27). These loops exhibited negligible changes, confirming that the resistive switching does not stem from charge absorption/desorption. Figure 4f shows the stable V_p dependence of the resistance. The device has a high HRS/LRS resistance ratio of nearly 100. After several pulsed voltages are applied, the I_{ds} - V_{ds} curves still remain almost linear but have different slopes (inset in Fig. 4f). Continuous-variable resistive states are achieved by pulsed gate voltages and are attributed to the moving and switching of multi-domains. To eliminate the interference from oxidation reactions, energy dispersive spectroscopy analysis was conducted on both Te and TeO_x nanowires, revealing a very low oxygen concentration in the Te nanowires (Supplementary Fig. 28 and Note 13). Through a series of measurements using PFM and resistive switching performances (Supplementary Figs. 29 and 30), no signs of ferroelectricity or resistive switching were observed in TeO_x nanowires, effectively ruling out the impact of oxidation reactions on the observed phenomena. Moreover, given that the region where Te nanowires can sustain ferroelectricity is able to be as small as ~22.5 nm, the storage density of SF-FETs prepared based on this ferroelectric property can reach $-1.92 \text{ TB}/\text{cm}^2$. The device, featuring continuous-variable resistive states and ultrahigh data density can be integrated with silicon circuits to achieve CMOS-compatible neuromorphic devices through 3D heterogeneous integration. This approach provides a foundational building block for broad-edge intelligence applications.

Discussion

To summarize, we have discovered a room-temperature vertical ferroelectricity in Te nanowire, a single-element material Te. A polar structure was detected through the STEM, resulting from a non-centrosymmetric lattice. PFM is used to probe the piezoelectric characteristics, hysteresis behaviors, and field-driven domain reversal. Based on the DFT simulations, the observed ferroelectric polarization can be attributed to off-center ion displacements along the inclined edge surface of Te. Moreover, as a ferroelectric semiconductor, Te nanowires possess high mobility along the Te chains and vertical ferroelectricity, which can be employed to realize a SF-FET device. Such device with fewer interfaces, demonstrate nonvolatile resistive switching, continuous-variable resistive states, ultrafast switching speed, and high-density storage, making them appropriate building blocks for in-memory computing. Our work expands the scope of ferroelectric materials and establishes a platform for ultrahigh-density memories and edge computing.

Methods

Materials synthesis

Te nanowires and nanosheets were synthesized using a substrate-free solution method (Supplementary Fig. 1). At first, Na_2TeO_3 (46 mg) and polyvinylpyrrolidone (PVP) (0.2 g) were mixed with double-distilled water (16 mL) at room temperature. To get a better mix, this solution was stirred with a magnetic stirrer for 20 min. Second, the solution was added with 1.66 mL of ammonia solution (25%, wt/wt %) and 0.84 mL of hydrazine hydrate (80%, wt/wt %). Finally, the above solution was transferred into a Teflon-lined stainless-steel autoclave and heated to a constant reaction temperature of 160 °C. After a set period of heating, the autoclave was naturally cooled down to room temperature. The silver-gray products of Te crystal can be precipitated by centrifugation at 4000 r/min for 15 min. To obtain a suspension of the Te nanowires or nanosheets, the solution was washed by centrifugation with distilled water three times.

The controls of PVP concentration and reaction time play an important role in obtaining different morphology of Te crystal (e.g., nanowires vs nanosheets). For all PVP concentrations, the initial

growth products are dominantly 1D nanostructures. After a certain period of reaction, Te nanosheet tend to emerge. Therefore, different Te structures can be formed by adjusting the experimental procedure. When different heating time was set to get different morphology, the time of 10 and 83 h is taken for Te nanowires and nanosheets, respectively.

Characterizations

Raman measurements were performed using a LabRAM HR Evolution Raman system with a green excitation laser of 532 nm. The TEM and Cs-corrected STEM images were obtained on a JEM-200CX and a FEI Titan3 G2 Cube (60–300 kV) with double Cs correctors in the TEM and STEM modes. The cross-sectional STEM samples were fabricated using the FEI Helios 600i dual-beam focused ion beam (FIB) system. Samples are generally transferred onto small copper grids covered with a thin carbon film. AFM and PFM measurements were carried out at the same time in a Bruker Multimode VIII instrument.

Piezoresponse force microscopy measurements

The samples for vertical PFM measurements were fabricated by transferring the Te nanowire and nanosheet onto Au-coated SiO_2 (285 nm)/Si substrates and *N*-doped conductive silicon (Si) substrates. The vertical PFM measurements were performed in the contact mode with Multimode VIII and ICON instruments (Bruker) and Asylum Research MFP-3D (Oxford) at room temperature. A PFM tip (SCM-PIT-V2) with force constant of around 2.8 N m^{-1} and contact resonance frequency of around 370 kHz was used in the PFM measurements by Bruker instruments. The contact strength was set to be lower than 10 nN to avoid unintentional damage. PFM tip (EFM-50, Nanoworld) was also used for the measurements of domain and polarization switching by Asylum Research MFP-3D. The tip has the same force constant ($\sim 2.8 \text{ N m}^{-1}$) and contact resonance frequency ($\sim 370 \text{ kHz}$) as the one of SCM-PIT-V2.

An AC bias voltage (V_{AC}) was used to drive the PFM tip, whose response (both amplitude and phase lag from the drive) were recorded. And then, the PFM tip needs to carry a constant DC voltage (V_{DC}) while being moved in contact mode across the Te surface. This applied external electric field generated by V_{DC} will cause the switching (or “poling”) of ferroelectric domains. By changing V_{DC} at different locations, ferroelectric domain patterns can be formed. This domain pattern can be observed by PFM in its amplitude and phase mapping images. Therefore, these images can be used to detect the movement and reversal of ferroelectric domain in Te nanowire and nanosheet.

PFM hysteresis measurements were used to verify the ferroelectricity. We changed the above constant V_{DC} into alternating “on” (during which V_{DC} was held constant) and “off” ($V_{DC} = 0 \text{ V}$) periods (each period has a duration of 20 ms), where the consecutive “on” values of step is through a (discretized) triangular waveform (Supplementary Fig. 2b). Therefore, ON- and OFF-field PFM mode can be realized in the on- and off-periods of V_{DC} -sweeping, respectively. The piezoresponse data collected in the on-period (or off-period) are used to plot ON-field (or OFF-field) phase and amplitude hysteresis loops.

Device fabrication and electrical measurements

The as-prepared Te nanowire and nanosheet can be easily transferred onto (90 nm) SiO_2/Si substrates. We transferred *h*-BN as a gate dielectric using poly(bisphenol A carbonate) film on polydimethylsiloxane. The *h*-BN flake was picked up at 70 °C and released at 170 °C. This stacking of heterostructure (*h*-BN/Te) was followed by the evaporation of the top gates of Au/Ti onto *h*-BN, the edge contact to *h*-BN/Te with Au/Ti with e-beam lithographic techniques and magnetron sputtering (Fig. 4a for a device schematic; some of our devices have two top gates slightly offset to the side away from the Te nanowire and not directly on top to reduce gate leakage, in this case the two

top gates are shorted together and connected to the same gate voltage thus acting as one gate).

Our devices for electrical measurements were wire-bonded with aluminum wire for transport measurement. Two-probe DC measurements were used because of the high resistance ($>1\text{ M}\Omega$) of few-layer Te nanowires. The transport measurements between drain/source electrodes were conducted along the c -axis of Te nanowire or nanosheet. The carriers in the channel can be induced and modulated by the top gate. The electrical transport measurements were performed with source meters (Keithley: Model 6517B). Top gate voltage pulses were applied with source meters (Keithley: Model 2400). For channel resistance (R_{ds}) vs gate voltage (V_g) curves (e.g., Fig. 4b), each R_{ds} was measured by waiting for 1 s after changing the gate voltage value (V_g) to exclude the hysteresis originating from the measurement lag. The nonvolatile resistive memory effects with multiple high and low resistive states were performed with a constant voltage of 0.5 V between drain and source electrodes. For R_{ds} vs V_p hysteresis loops (Fig. 4e), these resistive states were measured by waiting for 1 min after different voltage pulses (V_p) with pulse duration of 100 ms, which can exclude effects due to the measurement lag and the leakage current. Pulsed voltages with different amplitudes were carried out to produce multilevel resistive states. Multilevel R_{ds} can be switched reproducibly between high and low resistive states ($V_{ds} = 0.5\text{ V}$). Such continuous-variable resistive states can be fundamentally attributed to the nature of multidomain switching dynamics in the single-element ferroelectric Te nanowire. The degree of polarization can be increased with the increasing amplitude of pulsed voltage in a certain direction, which leads to the continuous-variable resistive states.

First-principles calculations

Our first-principles calculations were performed using the projected augmented wave (PAW)⁴⁶ formalism based on DFT, as implemented in the Vienna ab-initio simulation package (VASP)⁴⁷. The structural optimizations for α -state bulk Te are performed using SCAN⁴⁸, PBE⁴⁹, and various kinds of vdW functionals^{50–52} (DFT-D2, vdW-DF, optPBE-vdW, optB88-vdW, optB86b-vdW, and vdW-DF2). The SCAN functional is in the best agreement with experiments, as listed in Supplementary Table S1. Therefore, the SCAN functional is adopted in all calculations for geometric optimization. The cutoff energy of the plane-wave and the convergence criterion for the total energy were set to be 550 eV and 10^{-6} eV, respectively. The vacuum space of 20 Å was used to avoid the interaction between adjacent slabs. Atomic structures are fully relaxed until the Hellmann–Feynman force on each atom was smaller than 0.01 eV/Å. The Monkhorst–Pack k -point grids of $15 \times 15 \times 11$ and $1 \times 15 \times 11$ were employed to sample the first Brillouin zone of the α -state bulk and layered Te, respectively. The band structures of the α -state bulk and layered Te were calculated using the HSE06 functional⁵³ and the SOC was taken into consideration. The climbing image nudged elastic method⁵⁴ was used to calculate the energy barrier and the ferroelectric switching pathway of the layered Te from state α to state α' . The electric polarization of the α -state layered Te was calculated using the Berry phase method⁵⁵, as implemented in VASP.

Data availability

All data generated and analyzed in this study are included in the article and Supplementary Information and are also available at the corresponding authors' request.

References

- Yasuda, K., Wang, X., Watanabe, K., Taniguchi, T. & Jarillo-Herrero, P. Stacking-engineered ferroelectricity in bilayer boron nitride. *Science* **372**, 1458–1462 (2021).
- Qian, Z., Zhou, J., Wang, H. & Liu, S. Shift current response in elemental two-dimensional ferroelectrics. *npj Comput. Mater.* **9**, 67 (2023).
- Gou, J. et al. Two-dimensional ferroelectricity in a single-element bismuth monolayer. *Nature* **617**, 67–72 (2023).
- Fu, D.-W. et al. Diisopropylammonium bromide is a high-temperature molecular ferroelectric crystal. *Science* **339**, 425–428 (2013).
- Chanthbouala, A. et al. Solid-state memories based on ferroelectric tunnel junctions. *Nat. Nanotechnol.* **7**, 101–104 (2012).
- Vizner Stern, M. et al. Interfacial ferroelectricity by van der Waals sliding. *Science* **372**, 1462–1466 (2021).
- Liu, F. et al. Room-temperature ferroelectricity in CuInP_2S_6 ultrathin flakes. *Nat. Commun.* **7**, 12357 (2016).
- Ji, D. et al. Freestanding crystalline oxide perovskites down to the monolayer limit. *Nature* **570**, 87–90 (2019).
- Garcia, V. et al. Giant tunnel electroresistance for non-destructive readout of ferroelectric states. *Nature* **460**, 81–84 (2009).
- Si, M., Liao, P. Y., Qiu, G., Duan, Y. & Ye, P. D. Ferroelectric field-effect transistors based on MoS_2 and CuInP_2S_6 two-dimensional van der Waals heterostructure. *ACS Nano* **12**, 6700–6705 (2018).
- Si, M. et al. Steep-slope hysteresis-free negative capacitance MoS_2 transistors. *Nat. Nanotechnol.* **13**, 24–28 (2018).
- Yan, J. M. et al. Optoelectronic coincidence detection with two-dimensional $\text{Bi}_2\text{O}_2\text{Se}$ ferroelectric field-effect transistors. *Adv. Funct. Mater.* **31**, 2103982 (2021).
- Shen, P.-C., Lin, C., Wang, H., Teo, K. H. & Kong, J. Ferroelectric memory field-effect transistors using CVD monolayer MoS_2 as resistive switching channel. *Appl. Phys. Lett.* **116**, 033501 (2020).
- Zhao, X.-W. et al. Reversible and nonvolatile ferroelectric control of two-dimensional electronic transport properties of ZrCuSiAs -type copper oxyselenide thin films with a layered structure. *Phys. Rev. Mater.* **2**, 055003 (2018).
- Li, D. et al. Giant transport anisotropy in ReS_2 revealed via nanoscale conducting-path control. *Phys. Rev. Lett.* **127**, 136803 (2021).
- Hou, W. et al. Strain-based room-temperature non-volatile MoTe_2 ferroelectric phase change transistor. *Nat. Nanotechnol.* **14**, 668–673 (2019).
- Si, M. et al. A ferroelectric semiconductor field-effect transistor. *Nat. Electron.* **2**, 580–586 (2019).
- Wan, Y. et al. Room-temperature ferroelectricity in 1T'- ReS_2 multilayers. *Phys. Rev. Lett.* **128**, 067601 (2022).
- Weston, A. et al. Interfacial ferroelectricity in marginally twisted 2D semiconductors. *Nat. Nanotechnol.* **17**, 390–395 (2022).
- Rogee, L. et al. Ferroelectricity in untwisted heterobilayers of transition metal dichalcogenides. *Science* **376**, 973–978 (2022).
- Ding, W.-J. et al. Prediction of intrinsic two-dimensional ferroelectrics in In_2Se_3 and other $\text{III}_2\text{-VI}_3$ van der Waals materials. *Nat. Commun.* **8**, 14956 (2017).
- Wang, X. et al. Interfacial ferroelectricity in rhombohedral-stacked bilayer transition metal dichalcogenides. *Nat. Nanotechnol.* **17**, 367–371 (2022).
- Yang, D. et al. Spontaneous-polarization-induced photovoltaic effect in rhombohedrally stacked MoS_2 . *Nat. Photonics* **16**, 469–474 (2022).
- Fei, Z. et al. Ferroelectric switching of a two-dimensional metal. *Nature* **560**, 336–339 (2018).
- Wang, J. et al. Epitaxial BiFeO_3 multiferroic thin film heterostructures. *Science* **299**, 1719–1722 (2003).
- Wu, J. B. et al. High tunnelling electroresistance in a ferroelectric van der Waals heterojunction via giant barrier height modulation. *Nat. Electron.* **3**, 466–472 (2020).
- Zhao, R. et al. Emergent multiferroism with magnetodielectric coupling in EuTiO_3 created by a negative pressure control of strong spin-phonon coupling. *Nat. Commun.* **13**, 2364 (2022).

28. Qi, L., Ruan, S. & Zeng, Y. J. Review on recent developments in 2D ferroelectrics: theories and applications. *Adv. Mater.* **33**, 2005098 (2021).
29. Xiao, C. et al. Elemental ferroelectricity and antiferroelectricity in Group-V monolayer. *Adv. Funct. Mater.* **28**, 1707383 (2018).
30. Wang, Y. et al. Two-dimensional ferroelectricity and switchable spin-textures in ultra-thin elemental Te multilayers. *Mater. Horiz.* **5**, 521–528 (2018).
31. Qiu, G. et al. The resurrection of tellurium as an elemental two-dimensional semiconductor. *npj 2D Mater. Appl.* **6**, 17 (2022).
32. Zhou, G. et al. High-mobility helical tellurium field-effect transistors enabled by transfer-free, low-temperature direct growth. *Adv. Mater.* **30**, 1803109 (2018).
33. Qin, J.-K. et al. Raman response and transport properties of tellurium atomic chains encapsulated in nanotubes. *Nat. Electron.* **3**, 141–147 (2020).
34. Liang, F. X. & Qian, H. S. Synthesis of tellurium nanowires and their transport property. *Mater. Chem. Phys.* **113**, 523–526 (2009).
35. Dong, Z. & Ma, Y. Atomic-level handedness determination of chiral crystals using aberration-corrected scanning transmission electron microscopy. *Nat. Commun.* **11**, 1588 (2020).
36. Rao, G. F. et al. Robust piezoelectricity with spontaneous polarization in monolayer tellurene and multilayer tellurium film at room temperature for reliable memory. *Adv. Mater.* **34**, 2204697 (2022).
37. Calavalle, F. et al. Gate-tuneable and chirality-dependent charge-to-spin conversion in tellurium nanowires. *Nat. Mater.* **21**, 526–532 (2022).
38. Zhang, N. et al. Magnetotransport signatures of Weyl physics and discrete scale invariance in the elemental semiconductor tellurium. *Proc. Natl. Acad. Sci. USA* **117**, 11337–11343 (2020).
39. Qiu, G. et al. Quantum Hall effect of Weyl fermions in n-type semiconducting tellurene. *Nat. Nano.* **15**, 585–591 (2020).
40. Apte, A. et al. Piezo-response in two-dimensional α -Tellurene films. *Mater. Today* **44**, 40–47 (2021).
41. Wang, Y. et al. Field-effect transistors made from solution-grown two-dimensional tellurene. *Nat. Electron.* **1**, 228–236 (2018).
42. Gong, S. et al. Mixed dimensional Te nanowire-Te nanosheet heterojunctions with 2D electron gas on SrTiO₃ for diode applications. *ACS Appl. Nano Mater.* **4**, 10477–10484 (2021).
43. Li, L. et al. Black phosphorus field-effect transistors. *Nat. Nanotechnol.* **9**, 372–377 (2014).
44. Kim, S. et al. High-mobility and low-power thin-film transistors based on multilayer MoS₂ crystals. *Nat. Commun.* **3**, 1011 (2012).
45. Ma, C. et al. Sub-nanosecond memristor based on ferroelectric tunnel junction. *Nat. Commun.* **11**, 1439 (2020).
46. Blöchl, P. E. Projector augmented-wave method. *Phys. Rev. B* **50**, 17953 (1994).
47. Kresse, G. & Furthmüller, J. Efficient iterative schemes for ab initio total-energy calculations using a plane-wave basis set. *Phys. Rev. B* **54**, 11169 (1996).
48. Sun, J., Ruzsinszky, W. A. & Perdew, J. P. Strongly constrained and appropriately normed semilocal density functional. *Phys. Rev. Lett.* **115**, 036402 (2015).
49. Perdew, J. P., Burke, K. & Ernzerhof, M. Generalized gradient approximation made simple. *Phys. Rev. Lett.* **77**, 3865 (1996).
50. Grimme, S. Semiempirical GGA-type density functional constructed with a long-range dispersion correction. *J. Comput. Chem.* **27**, 1787 (2006).
51. Klimeš, J., Bowler, D. R. & Michaelides, A. Chemical accuracy for the van der Waals density functional. *J. Phys. Condens. Matter* **22**, 022201 (2010).
52. Klimeš, J. D., Bowler, R. & Michaelides, A. Van der Waals density functionals applied to solids. *Phys. Rev. B* **83**, 195131 (2011).
53. Heyd, J., Scuseria, G. E. & Ernzerhof, M. Hybrid functionals based on a screened Coulomb potential. *J. Chem. Phys.* **118**, 8207 (2003).
54. Henkelman, G., Uberuaga, B. P. & Jonsson, H. A climbing image nudged elastic band method for finding saddle points and minimum energy paths. *J. Chem. Phys.* **113**, 9901–9904 (2000).
55. King-Smith, R. D. & Vanderbilt, D. Theory of polarization of crystalline solids. *Phys. Rev. B* **47**, 1651–1654 (1993).

Acknowledgements

We thank Z. B. Hu and H. Ma for helpful discussions and C. L. Liu for experimental support. This work was supported by the National Natural Science Foundation of China (Grant No. 12274316, 11974304, 62004136, 11904250, 12474014), and the National Science Foundation of Jiangsu Higher Education Institutions (20KJB140019), and also by Doctor of Entrepreneurship and Innovation in Jiangsu Province (No. (2020)30790). Y.P.Q. thanks Macau Science and Technology Development Fund (FDCT Grants 0031/2021/ITP) and the JSPS KAKENHI (22H00278). X.R.W. also thanks the National Key R&D Program of China (2022YFB4400100, 2023YFF1500500), the National Natural Science Foundation of China (T2221003), and the Leading-Edge Technology Program of Jiangsu Natural Science Foundation (BK20232024). Y.P.Q. acknowledges support by Tohoku University TUMUG Startup Research FUND, FY2023 AIMR Fusion Research Fund, and AIMR Overseas Dispatch Program for Young Researchers FY2023. M.A.S., D.S., and Y.P.C. also acknowledge support by Purdue University, and Multidisciplinary University Research Initiatives (MURI) program (FA9550-20-1-0322) led by University of Southern California.

Author contributions

Y.C.J. conceived the idea and designed the experiments; Y.C.J. and Y.P.C. supervised the project and coordinated the collaboration; S.N.G. grew the Te crystals and fabricated the devices; S.N.G., Y.C.J., J.L.Z., H.X., Z.Q.L., R.Z., M.A.S., D.S. and D.P.C. performed the electrical and optical measurements; Y.C.J. and H.B.Y. were responsible for the TEM measurements; J.Y.Z. and C.L.M. performed DFT calculations; Y.C.J., X.R.W., Y.P.C., R.Z., Y.P.Q., Z.P.W., L.W., X.S.W. and J.G. analyzed the data and interpreted the experimental results; J.L.Z., Y.C.J., J.Y.Z., X.R.W. and Y.P.Q. wrote the manuscript. All authors discussed the results and commented on the manuscript.

Competing interests

The authors declare no competing interests.

Additional information

Supplementary information The online version contains supplementary material available at <https://doi.org/10.1038/s41467-024-52062-6>.

Correspondence and requests for materials should be addressed to Yong P. Chen, Xinran Wang or Yucheng Jiang.

Peer review information *Nature Communications* thanks Siddhartha Ghosh, Chenqiang Hua, and Wenwu Li for their contribution to the peer review of this work. A peer review file is available.

Reprints and permissions information is available at <http://www.nature.com/reprints>

Publisher's note Springer Nature remains neutral with regard to jurisdictional claims in published maps and institutional affiliations.

Open Access This article is licensed under a Creative Commons Attribution-NonCommercial-NoDerivatives 4.0 International License, which permits any non-commercial use, sharing, distribution and reproduction in any medium or format, as long as you give appropriate credit to the original author(s) and the source, provide a link to the Creative Commons licence, and indicate if you modified the licensed material. You do not have permission under this licence to share adapted material derived from this article or parts of it. The images or other third party material in this article are included in the article's Creative Commons licence, unless indicated otherwise in a credit line to the material. If material is not included in the article's Creative Commons licence and your intended use is not permitted by statutory regulation or exceeds the permitted use, you will need to obtain permission directly from the copyright holder. To view a copy of this licence, visit <http://creativecommons.org/licenses/by-nc-nd/4.0/>.

© The Author(s) 2024

¹Key Laboratory of Intelligent Optoelectronic Devices and Chips of Jiangsu Higher Education Institutions, School of Physical Science and Technology, Suzhou University of Science and Technology, Suzhou, China. ²Advanced Technology Research Institute of Taihu Photon Center, School of Physical Science and Technology, Suzhou University of Science and Technology, Suzhou, China. ³Laboratory of Solid State Microstructures, Nanjing University, Nanjing, China. ⁴Department of Engineering Science, Faculty of Innovation Engineering, Macau University of Science and Technology, Macau SAR, China. ⁵Advanced Institute for Materials Research, Tohoku University, Sendai, Japan. ⁶Department of Physics and Astronomy and Elmore Family School of Electrical and Computer Engineering and Birk Nanotechnology Center and Purdue Quantum Science and Engineering Institute, Purdue University, West Lafayette, IN, USA. ⁷Institute of Materials Science & Devices, Suzhou University of Science and Technology, Suzhou, China. ⁸State Key Laboratory of Information Photonics and Optical Communications & School of Science, Beijing University of Posts and Telecommunications, Beijing, China. ⁹Department of Physics and Astronomy, University of Tennessee, Knoxville, TN, USA. ¹⁰School of Materials Science and Engineering, Shanghai University, Shanghai, China. ¹¹School for Optoelectronic Engineering, Zaozhuang University, ZaoZhuang, Shandong, China. ¹²Institute of Physics and Astronomy and Villum Center for Hybrid Quantum Materials and Devices, Aarhus University, Aarhus, Denmark. ¹³School of Integrated Circuits, Nanjing University, Suzhou, China. ¹⁴National Laboratory of Solid State Microstructures, School of Electronic Science and Engineering and Collaborative Innovation Center of Advanced Microstructures, Nanjing University, Nanjing, China. ¹⁵Interdisciplinary Research Center for Future Intelligent Chips (Chip-X), Nanjing University, Suzhou, China. ¹⁶Suzhou Laboratory, Suzhou, China. ¹⁷These authors contributed equally: Jinlei Zhang, Jiayong Zhang, Yaping Qi, Shuainan Gong. ✉ e-mail: yongchen@purdue.edu; xrwang@nju.edu.cn; jyc@usts.edu.cn